Supplementary Information

for

Helical Perylene Diimide Self-Assembly with a Redox Active Molecular Switch Applied to Humidity Sensing

Li Zhang, [ab] *Li Yang,* [a] *Yining He* [ab] *and Ji-Min Han* *[ab]

[a] State Key Laboratory of Explosion Science and Technology, Beijing Institute of Technology, 5 Zhongguancun South Street, Haidian District, Beijing, 100081, China.

[b] Explosion Protection and Emergency Disposal Technology Engineering Research Center of the Ministry of Education, Beijing Institute of Technology, 5 Zhongguancun South Street, Haidian District, Beijing, 100081, China.

* Corresponding author: Dr. Ji-Min Han; E-mail: hanjimin@bit.edu.cn

Table of Contents

S1. Materials and General Methods

Unless otherwise stated, all reagents were purchased from commercial suppliers (Sigma-Aldrich or Fisher) and employed without further purification. Thin layer chromatography (TLC) was performed on silica gel 60 F254 (E. Merck). Column chromatography was carried out on silica gel 60F (Merck 9385, 0.040–0.063 mm). Nuclear magnetic resonance (NMR) spectra were recorded at 298 K on a Bruker Avance III 500 spectrometer, with a working frequency of 500 MHz for ^{1}H and 125 MHz for ^{13}C. Chemical shifts are listed in ppm on the δ scale and coupling constants are recorded in Hertz (Hz). Deuterated solvents for NMR spectroscopic analyses were used as received. Chemical shifts are reported in δ values relative to the signals corresponding to the residual non-deuterated solvents (CD_3CN: δ_H 1.94 ppm, δ_C 1.32 ppm, 118.26 ppm). High resolution mass spectra were measured on a Finnigan LCQ iontrap mass spectrometer (HR-ESI).

Powder X-ray diffraction (PXRD) patterns were collected at room temperature on a STOE-STADI MP powder diffractometer equipped with an asymmetric curved Germanium monochromator (CuKα1 radiation, λ = 1.54056 Å) and one-dimensional silicon strip detector (MYTHEN2 1K from DECTRIS). The line focused Cu X-ray tube was operated at 40 kV and 40 mA. Intensity data from 3 to 80 degrees two theta were collected over a period of 22 minutes. The instrument was calibrated against a NIST Silicon standard (640d) prior to the measurement.

Cyclic voltammetry (CV) experiments were carried out at room temperature in argon-purged MeCN or aqueous solutions with a Gamry Multipurpose instrument (Reference 600) interfaced to a PC. The samples were purged with Ar for 30 minutes before test. The simulation is generated using DigiSim 3.03b software purchased from BASi Company. The working electrode was a glassy carbon (0.071 cm^2) and the surface was polished routinely with 0.05 μm alumina-water slurry on a felt surface immediately before use. The counter electrode was a Pt coil and the reference electrode was Ag/AgCl electrode. The concentration of supporting electrolyte was 0.1 M tetrabutylammonium hexafluorophosphate (TBA•PF_6) in MeCN, or 0.1 M tetrabutylammonium chloride (TBA•Cl) in water.

Field-emission scanning electron microscope (FE-SEM) images were obtained on a Hitachi SU-8030 microscope operating at 1.0 kV. FE-SEM samples were prepared by drop-casting diluted PDI-DV suspension onto silicon native oxide substrates and allowed to dry for 4 hours. The samples for FE-SEM observations were prepared without any metal coating.

High Resolution Transmission Electron Microscopy (TEM) images were taken with a Hitachi 8100 microscope (Japan) operating at 200 kV. TEM samples were prepared by drop-casting diluted PDI-DV suspension onto substrates and allowed to dry for 4 hours. For TEM measurements, the samples were dispersed in ethanol and then dried on a holey carbon film Cu grid.

The adsorption experiments were measured with an Autosorb iQ Station 2 outfitted with the micropore option by Quantachrome Instruments. Water vapor sorption isotherms were measured with an automated Vstar 3-0000-1000-XS from Quantachrome Instruments.

S2. Synthesis

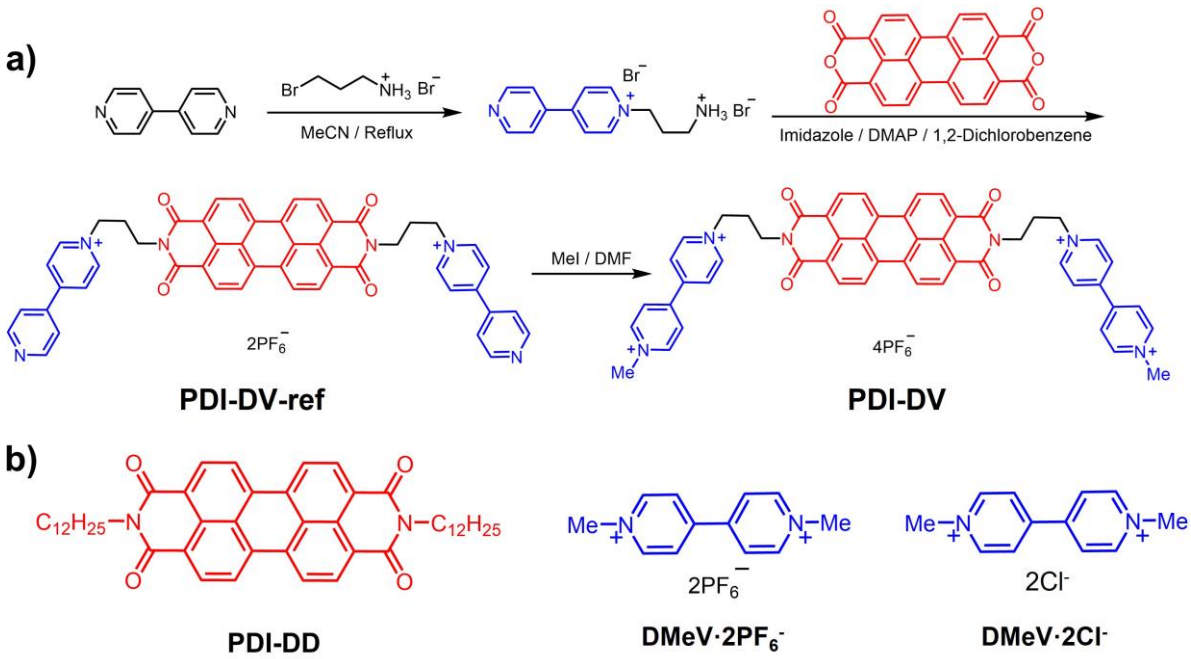

Scheme S1. a) Synthesis of **PDI-DV**. b) The reference compounds, **PDI-DD**, **DMeV•2PF6** and **DMeV•2Cl** employed in this work. The **DMeV•2PF6** and **DMeV•2Cl** were purchased from commercial suppliers.

1,1''-((1,3,8,10-Tetraoxo-1,3,8,10-tetrahydroanthra[2,1,9-def:6,5,10-d'e'f']diisoquinoline-2,9-diyl)bis(propane-3,1-diyl))bis([4,4'-bipyridin]-1-ium) bishexafluorophosphate

(PDI-DV-Ref•2PF6)

The compound was synthesized based on a modified procedure reported in the literature.[1] A mixture of perylene-3,4,9,10-tetracarboxylic dianhydride (100 mg, 0.255 mmol), 4-(4'-pyridyl)-1-(3-aminopropyl) pyridinium bromide hydrobromide salt (188 mg, 0.501 mmol), 4-dimethylaminopyridine (DMAP, 56 mg, 0.5 mmol), and imidazole (68 mg, 1 mmol) in *o*-dichlorobenzene (5 ml) was heated at 200 °C with stirring for 12 h. After cooling, the resulting precipitate was collected by filtration. The collected red solid was dissolved in H_2O (50 ml) and then the solution was washed with CH_2Cl_2 to remove H_2O insoluble residues. A portion of saturated aqueous ammonium hexafluorophospate solution (10 ml) was added to the separated water layer. The resulting red precipitate was collected by centrifugation, and washed with H_2O, EtOH and Et_2O to give **PDI-DV-Ref • 2PF6**. (180 mg, 0.168 mmol, 67%): ^{1}H NMR (500 MHz, CD_3SOCD_3); δ d 9.28 (d, *J* = 6.4 Hz, 4H), 8.86 (d, *J* = 4.8 Hz, 4H), 8.67 (d, *J* = 6.0 Hz, 4H), 8.44 (d, *J* =

8.4 Hz, 4H), 8.27 (d, *J* = 7.6 Hz, 4H), 8.01 (d, *J* = 5.2 Hz, 4H), 4.79 (br t, 4H), 4.26 (br s, 4H), 2.47 (br t, 4H). ^{13}CNMR (125 MHz, CD_3SOCD_3) d 164.2, 152.7, 151.4, 145.8, 141.0, 133.6, 130.9, 128.2, 125.7, 125.0, 124.3, 122.5, 122.2, 59.1, 37.4, 30.3. MS (ESIMS) *m/z.* 929.77 $(M - PF_6)^+$.

1',1'''-((1,3,8,10-tetraoxo-1,3,8,10-tetrahydroanthra[2,1,9-def:6,5,10-d'e'f']diisoquinoline-2,9-diyl)bis(propane-3,1-diyl))bis(1-methyl-[4,4'-bipyridine]-1,1'-diium) tetrahexafluorophosphate (PDI-DV•4PF$_6$)

A mixture of **PDI-DV-Ref•2PF$_6$** (100 mg, 0.09 mmol) and MeI (29 mg, 0.2 mmol) in MeCN (6 ml) was heated under reflux at 90 ^{o}C for 12 h. After cooling to room temperature, the resulting precipitate was collected by filtration and washed with MeCN. The collected red solid was dissolved in H_2O (50 ml) and then the solution was washed with CH_2Cl_2 to remove water insoluble residues. A portion of saturated aqueous ammonium hexafluorophospate solution (10 ml) was added to the separated water layer. The resulting red precipitate was collected by centrifugation, and washed with H_2O, EtOH and Et_2O to afford **PDI-DV•4PF$_6$**. The resulting red precipitates were dried under vacuum (40 mg, 0.029 mmol, 32%): ^{1}H NMR (500 MHz, CD_3CN); d 9.48 (d, *J* = 6.4 Hz, 4H), 9.33 (d, *J* = 6.0 Hz, 4H), 8.89 (d, *J* = 6.0 Hz, 4H), 8.82 (d, *J* = 6.0 Hz, 4H), 8.50 (d, *J* = 8.0 Hz, 4H), 8.29 (d, *J* = 7.6 Hz, 4H), 4.88 (br s, 4H), 4.48 (s, 6H), 4.29 (br s, 4H), 2.50 (br s, 4H). ^{13}C NMR (125 MHz, CD_3CN); d 163.2, 148.8, 148.3, 147.0, 146.3, 133.6, 130.8, 128.2, 126.9, 126.4, 125.0, 124.4, 122.5, 59.4, 48.5, 37.3, 30.5. MS (ESI-MS) *m/z*. 1249.08 $(M - PF_6)^+$.

1',1'''-((1,3,8,10-tetraoxo-1,3,8,10-tetrahydroanthra[2,1,9-def:6,5,10-d'e'f']diisoquinoline-2,9-diyl)bis(propane-3,1-diyl))bis(1-methyl-[4,4'-bipyridine]-1,1'-diium) tetrachloride

(PDI-DV•4Cl)

A solution of PDI-DV•4PF$_6$ (0.05 mmol) in methanol (3 ml) was mixed with a saturated methanol solution of potassium chloride (3 ml). The solid precipitation of PDI-DV•4Cl appeared after standing for several hours.

2,9-Didodecylanthra[2,1,9-def:6,5,10-d'e'f']diisoquinoline-1,3,8,10(2H,9H)-tetrone

(PDI-DD)

To a 50 mL round bottom flask was added 0.5 g (1.27 mmol) perylene-3,4,9,10-tetracarboxylic dianhydride, 6.0 g of imidazole, and 0.942 g (5.08 mmol) of *n*-dodecylamine. The reaction mixture was heated with stirring under N_2 at 180 ºC for 4 h and then allowed to cool to room temperature. Next, 50 mL of ethanol was added, followed by the addition of 100 mL of 2 M HCl. The mixture was next allowed to stir overnight. The red precipitate was collected by filtration, followed by washing with water and drying under vacuum. The crude product was then purified by chromatographed on silica (chloroform) to afford (0.72 g, 78%). ^{1}H NMR (500 MHz, $CDCl_3$); δ = 8.71 (d, 8 H, *J* =17.6 Hz), 4.22 (t, 4 H, *J* = 7.2 Hz), 1.58-0.89 (m, 46 H).

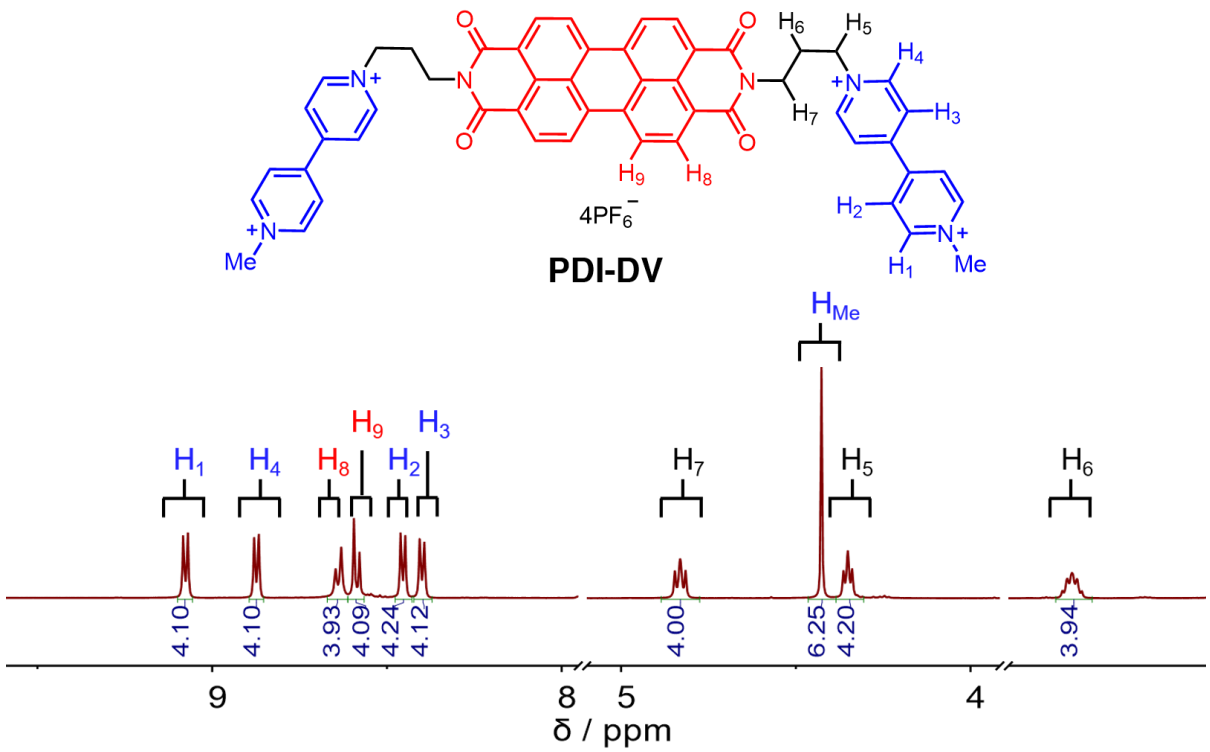

Fig. S1. ^{1}H NMR spectrum of **PDI-DV**

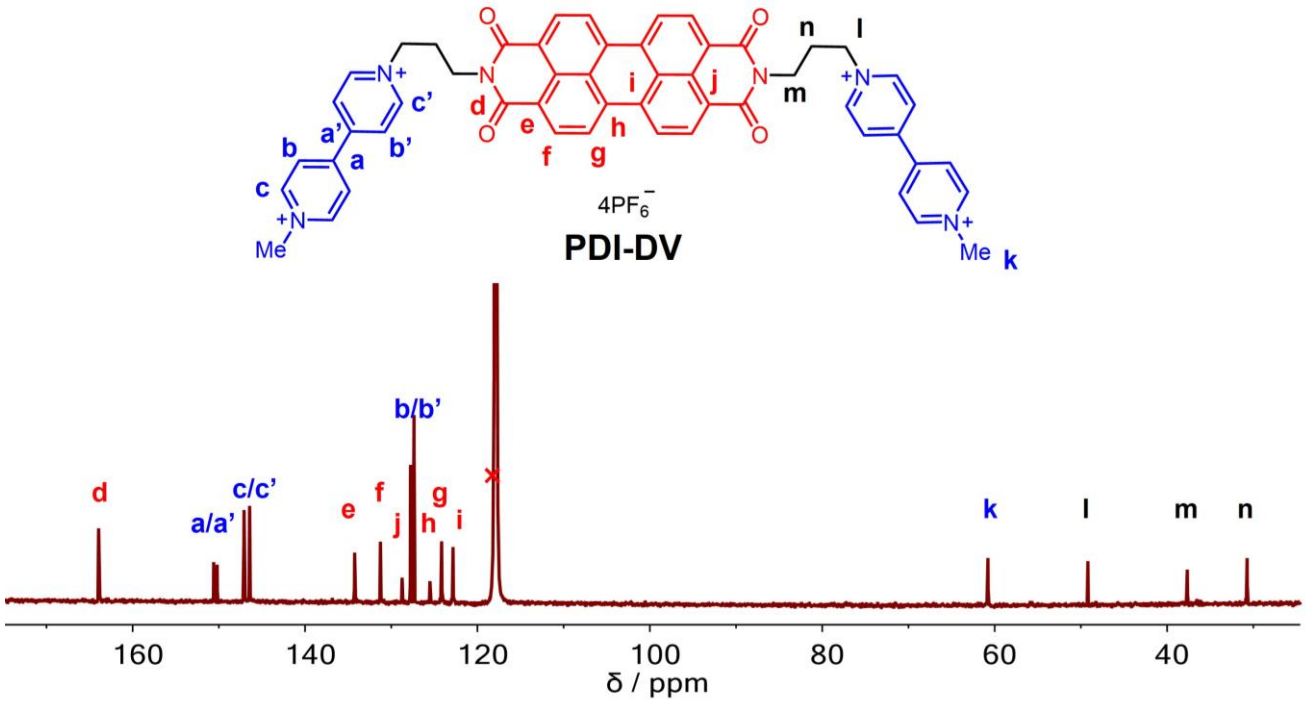

Fig. S2. ^{13}C NMR spectrum of **PDI-DV**

S3. Density Functional Theory Calculations

All density functional theory (DFT) calculations were performed at the cam-B3LYP/6-31G* level and utilized Polarizable Continuum Model (PCM) to incorporate the effect of solvent (MeCN or H_2O) with the Q-Chem 4.3 package.[2] Geometry optimizations were performed without symmetry constraints, and the subsequent vibrational analysis returned no imaginary frequencies. The molecular orbitals were generated with IQmol.

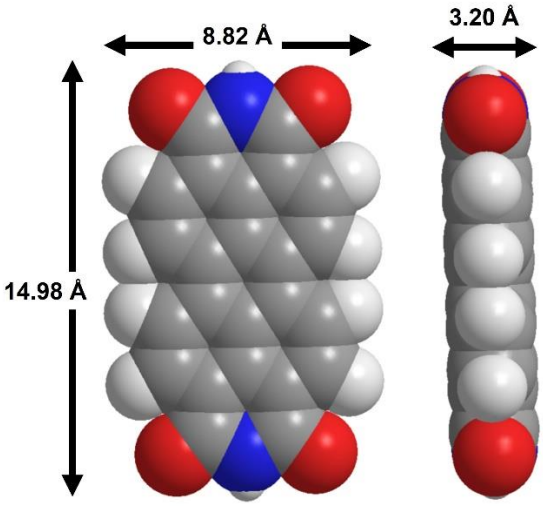

Fig. S3. The molecular structure of **PDI** displayed as space-filling mode. (Obtained from ChemDraw software. Gray: C; white: H; red: O; blue: N) The perimeters are given in Å.

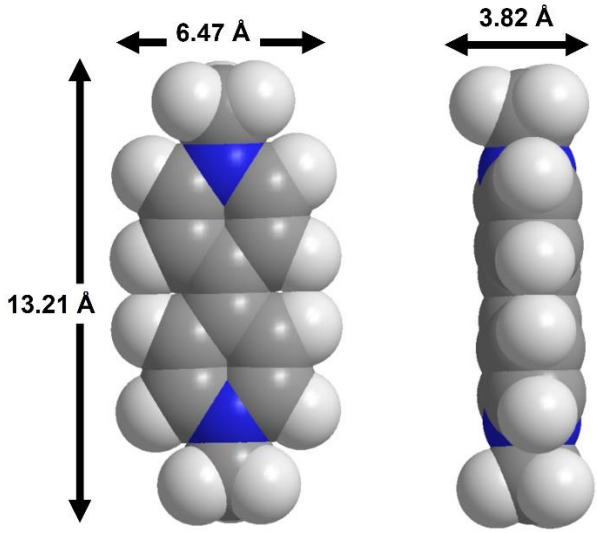

Fig. S4. The molecular structure of **DMeV** displayed as space-filling mode. (Obtained from ChemDraw software. Gray: C; white: H; red: O; blue: N) The perimeters are given in Å.

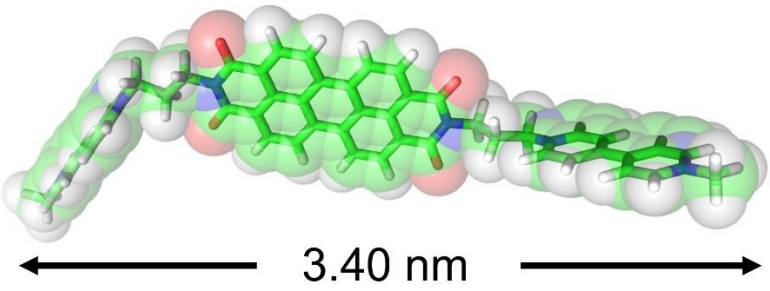

Fig. S5. The DFT simulated structure of **PDI-DV** at cam-B3LYP/6-31G*/PCM (MeCN solvent) level displayed as wireframe and space-filling mode. (Green: C; white: H; red: O; blue: N) The simulated structure indicates that the length of the PDI-DV molecule is about 3.4 nm.

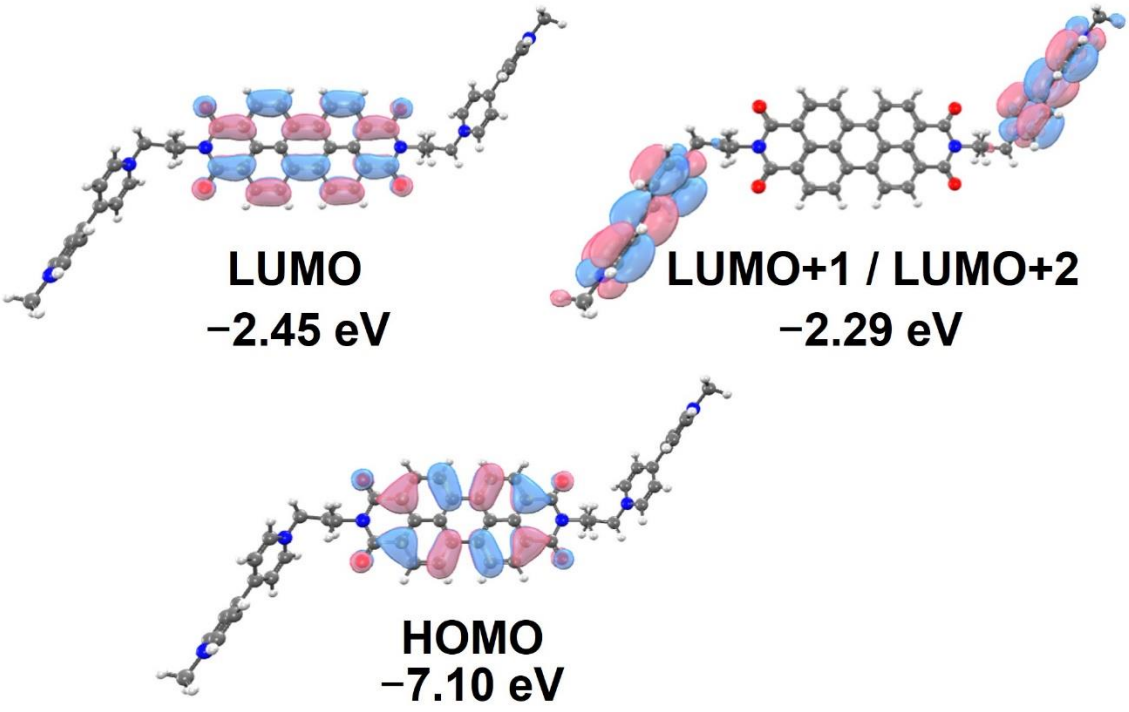

Fig. S6. The DFT calculated electron density distributions of the LUMO, HOMO and LUMO+1 / LUMO+2 orbitals for **PDI-DV** in MeCN.

S4. Atomic Force Microscopy

Atomic force microscopy (AFM) was performed by using a Bruker Dimension Icon operated in tapping mode using silicon cantilevers having either a nominal spring constant of 0.3 N/m (resonance frequency = 21 kHz) or 0.9 N/m (resonance frequency = 60 kHz). AFM images were acquired as 512 pixels × 512 pixels with a scan rate of 1.00 Hz.

Mica sample disks were used as the sample substrates and as an atomic resolution standard in all AFM analysis.

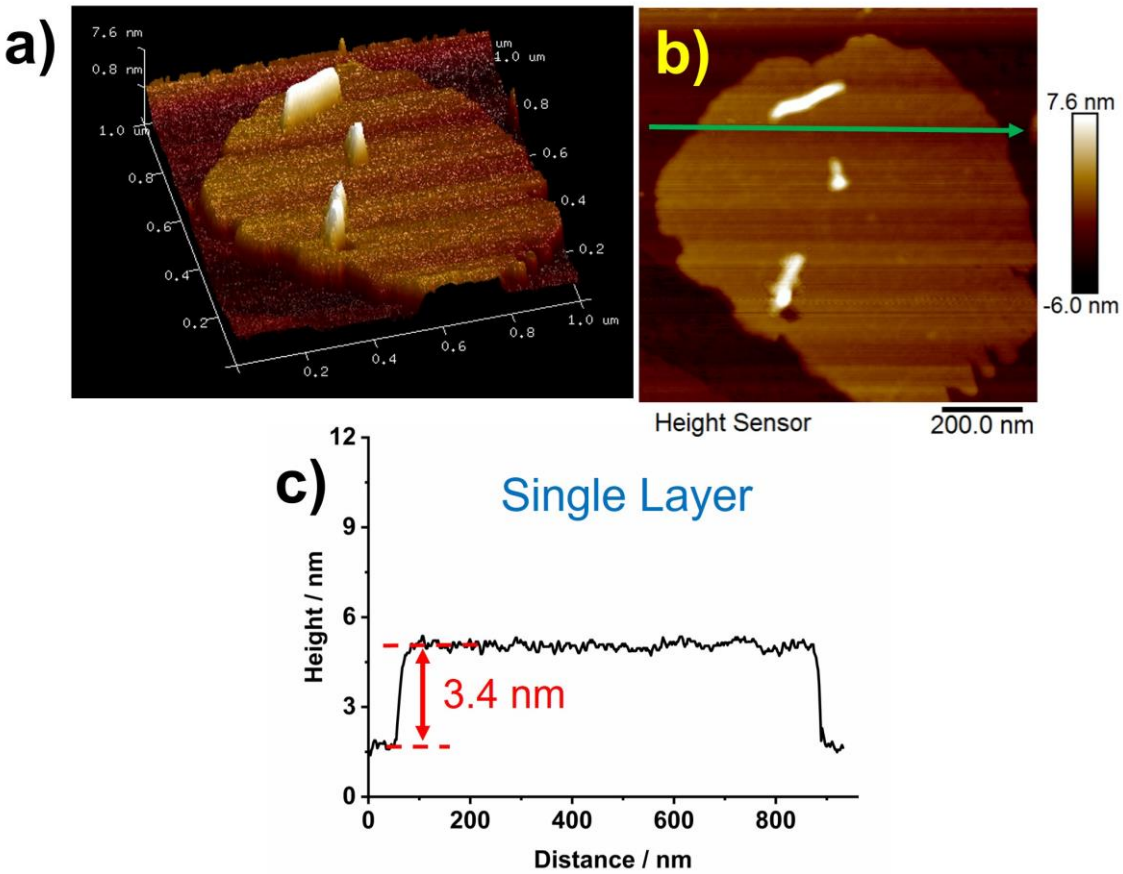

Fig. S7. The AFM height image of 0.5 mM **PDI-DV** MeCN solution drop-casted on the mica sample disk, showing in a) three-dimensional diagram and b) top view. c) Dependence of height on the distance (green arrow).

The 0.5 mM **PDI-DV** MeCN solution was drop-casted evenly on the mica sample disk and dried thoroughly. Due to polarity, the PDI cores tend to be farther away from the mica disk, and the PDI-DV molecule tends to "stand up", which means the height measured in the AFM experiment is roughly the

same as the molecule length. Shown in Fig. S7, the measured height is about 3.4 nm, indicating that the PDI-DV molecules formed a single layer structure on the mica sample disk.

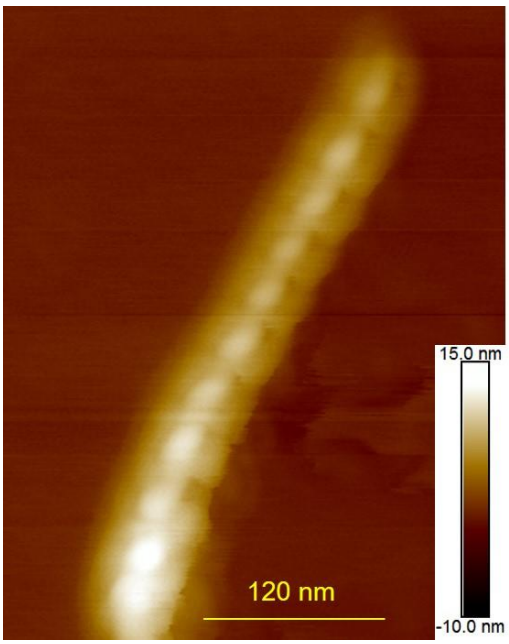

Fig. S8. The AFM height image of **PDI-DV** nanohelix fiber.

The AFM height image shows the helical structure of PDI-DV to a certain extent. However, due to its low resolution, more detailed information of the nanohelix cannot be obtained.

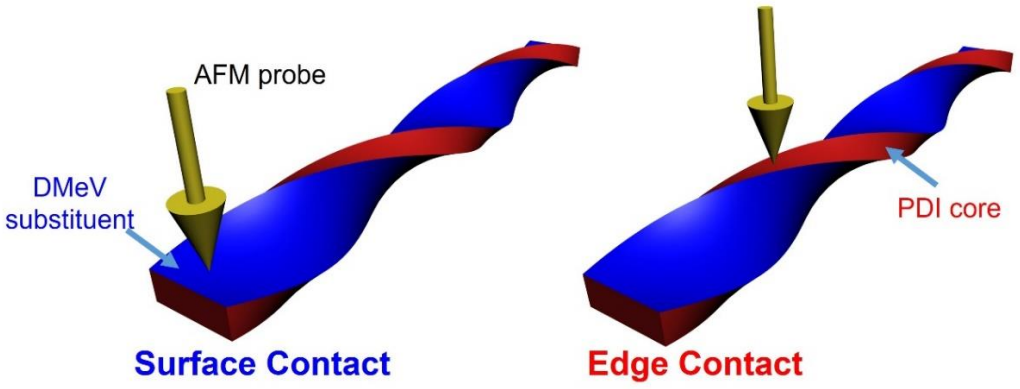

Fig. S9. The different contact mode between the AFM probe and the nanohelix in tapping mode.

S5. UV-Vis and Fluorescent Spectroscopy

UV-Vis-NIR Spectra were recorded on a Varian 100-Bio UV-Vis spectrophotometer in MeCN or aqueous solution at room temperature.

The quantum yields (Φ) of PDI-DV were determined by a single-point measurement with a standard sample of known quantum yield. *N*,*N*′-Bis(1-Hexylheptyl)-perylene-3,4:9,10-bis-dicarboximide (Φ = 0.99 ± 0.05 in CH_2Cl_2)[3] was chosen as standard sample for PDI-DV. The excitation wavelength was selected as 485 nm, and the emission peak was monitored at 529 nm. The quantum yield of **PDI-DV•4PF$_6$** in MeCN was determined as **0.380**, and the quantum yield of **PDI-DV•4Cl** in water was determined as **0.118**.

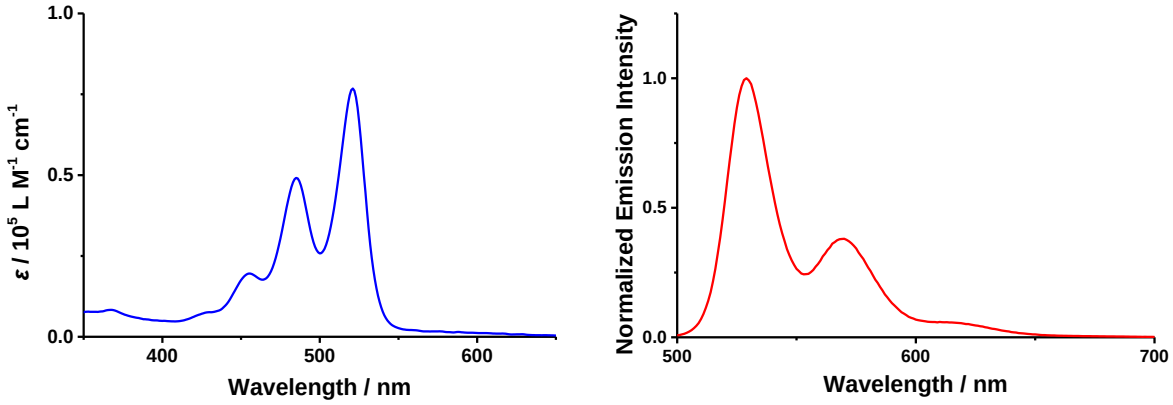

Fig. S10. Absorption and fluorescent spectra of the MeCN solution of **PDI-DV•4PF$_6$**

The UV-Vis absorption spectra recorded three prominent vibronic bands of **PDI-DV** in MeCN solution at 520, 485 and 455 nm attributed to the 0–0, 0–1, and 0–2 vibrational transitions. The fluorescent spectra recorded three emission peaks at 529, 570 and 621 nm, where the peak at 621 nm is the broad peak.

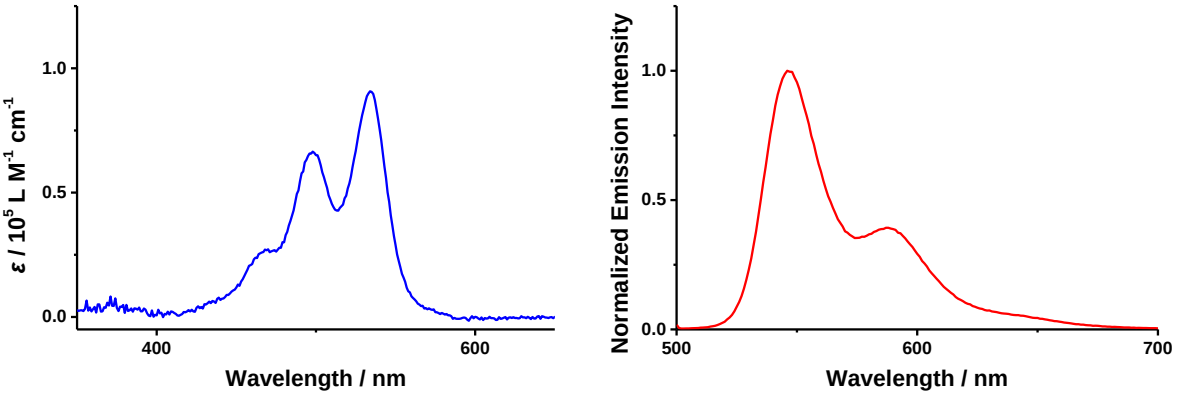

Fig. S11. Absorption and fluorescent spectra of the aqueous solution of **PDI-DV•4Cl**

The UV-Vis absorption spectra recorded three prominent vibronic bands of **PDI-DV** in H_2O at 535, 498 and 468 nm attributed to the 0–0, 0–1, and 0–2 vibrational transitions. The fluorescent spectra recorded three emission peaks at 547, 589 and 646 nm, where the peak at 646 nm is the broad peak.

S6. Contact Angles Measurements

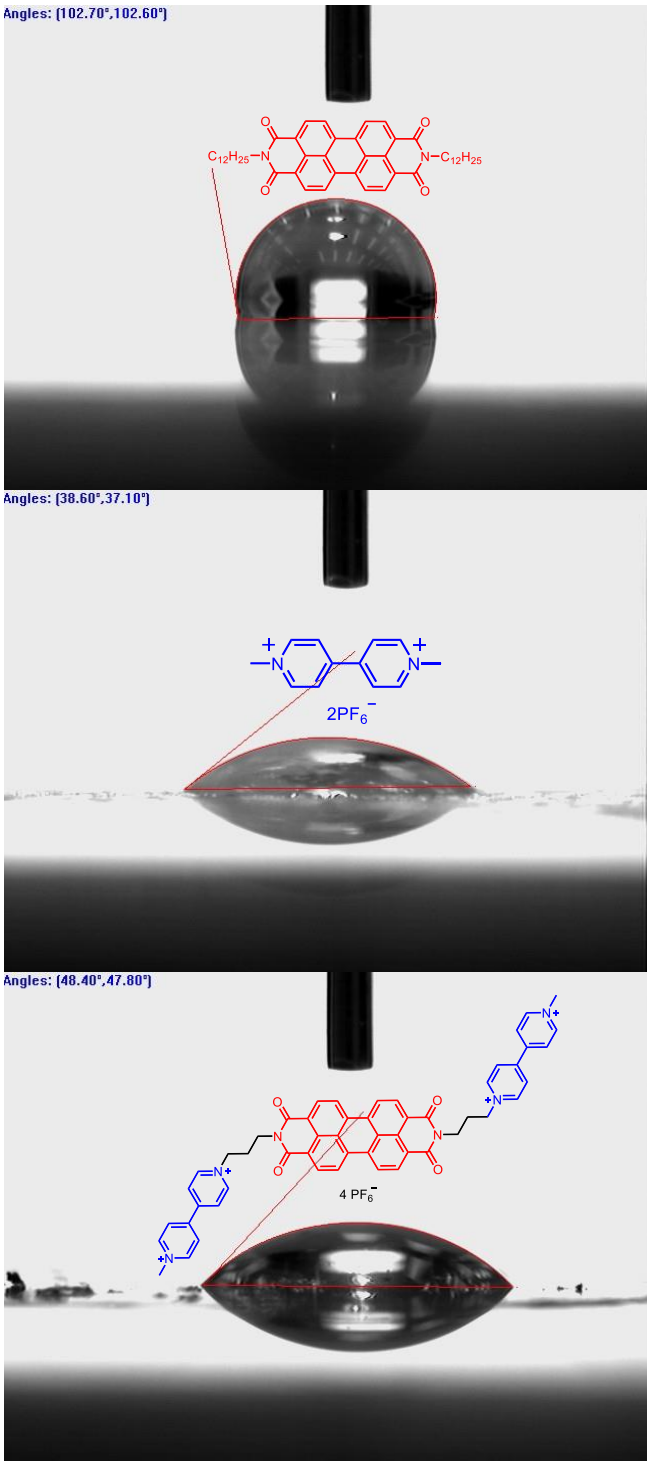

Fig. S12. Contact angles of a) **PDI-DD** (102.6° - 102.7°, hydrophobic surface), b) **DMeV•2PF$_6$** (37.1° -38.6°, hydrophilic surface), and c) **PDI-DV•4PF$_6$** (47.8° -48.4°, hydrophilic surface) measured on glass substrates.

Contact angles experiments were performed using The VCA Optima Contact Angle Measurement system. The micropipette is filled with de-ionized water, and placed within a plastic holder. The sample are fabricated on the glass substrates by drop-casting. The droplet is dispensed manually at the tip, as the stage raises the sample surface into contact with the liquid. Upon creating the droplet on the surface of the sample, the VCA software program captures the image on a CCD camera. The angles are measured by utilizing the software. The process was repeated for different locations on the sample.

S7. Femtosecond transient absorption Spectroscopy

The 525 nm photoexcitation pulses used in our measurements were obtained through a home-built optical parametric amplifier. The pulse power for photoexcitation was attenuated to ~1 μJ/pulse using neutral density filters. The pump polarization was randomized using a commercial depolarizer (DPU-25-A, Thorlabs, Inc.) to eliminate any orientational dynamics contributions from the experiment. Spectra were collected on a commercial spectrometer (Ultrafast Systems Helios). All samples were stirred to avoid localized heating or degradation effects. The optical density was maintained around 0.5 for all samples.

All transient absorption data were background-subtracted to remove scattered light and thermally lensed fluorescence from the spectra, and then corrected for group delay dispersion (GDD, or "chirp") using Surface Xplorer Pro 4 (Ultrafast Systems, LLC).

The kinetic analysis was performed using home written programs in MATLAB and was based on a global fit to selected single-wavelength kinetics. The time-resolution is given as w = 350 fs (full width at half maximum, FWHM); the assumption of a uniform instrument response across the frequency domain and a fixed time-zero (t_0) are implicit in global analysis.

The kinetic data from multiple different wavelengths are fit using the global analysis described below. Each wavelength is given an initial amplitude that is representative of the spectral intensity at time t_0, and varied independently to fit the data. The time/rate constants and t_0 are shared between the various kinetic data and are varied globally across the kinetic data in order to fit the model(s) described below. We globally fit the dataset to a specified kinetic model and use the resultant populations to deconvolute the dataset and reconstruct species-associated spectra.

We used the following first-order kinetic models with rate matrices K for the compounds and excitation wavelengths:

For the TA of **PDI-DV** and **PDI-DV-ref** in H_2O exciting at 525 nm:

$$\underline{\underline{K}} = \begin{pmatrix} -k_{S1-n} & 0 & 0 \\ 0 & -k_{relax-a} & 0 \\ 0 & k_{relax-a} & k_{S1-a} \end{pmatrix} \qquad \text{(Eqn. S1)}$$

in which $k_{S1\text{-}n}$ and $k_{S1\text{-}a}$ are the first excited state population decay rates for non-aggregated and aggregated species, respectively; $k_{relax\text{-}a}$ represents the ultrafast conformational relaxation rate for the aggregated species.

For the TA of **PDI-DV** and **PDI-DV-ref** in MeCN exciting at 525 nm:

$$\underline{\underline{K}} = \left(-k_{S1}\right) \qquad \text{(Eqn. S2)}$$

in which k_{S1} is the first excited state population decay rate.

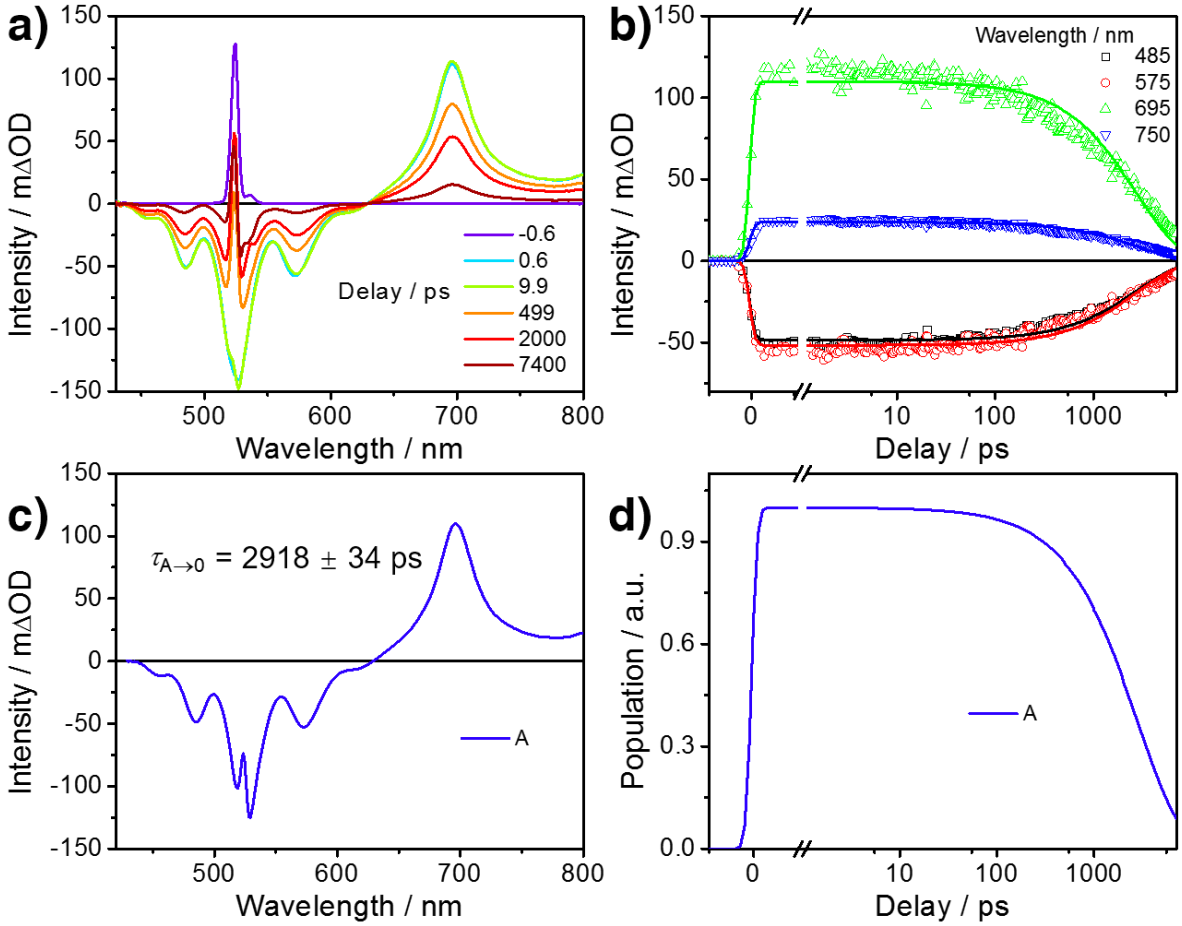

Fig. S13. Femtosecond transient absorption spectra of **PDI-DV-ref** in **MeCN** excited at 525 nm (~100 fs, 1 μJ/pulse). (a) Visible spectra. (b) Multiple wavelength fits. (c) Species associated spectrum and the time constant. (d) Population curve from transient absorption fit to first order decay model. Species A represents the singlet excited state of **PDI-DV-ref**.

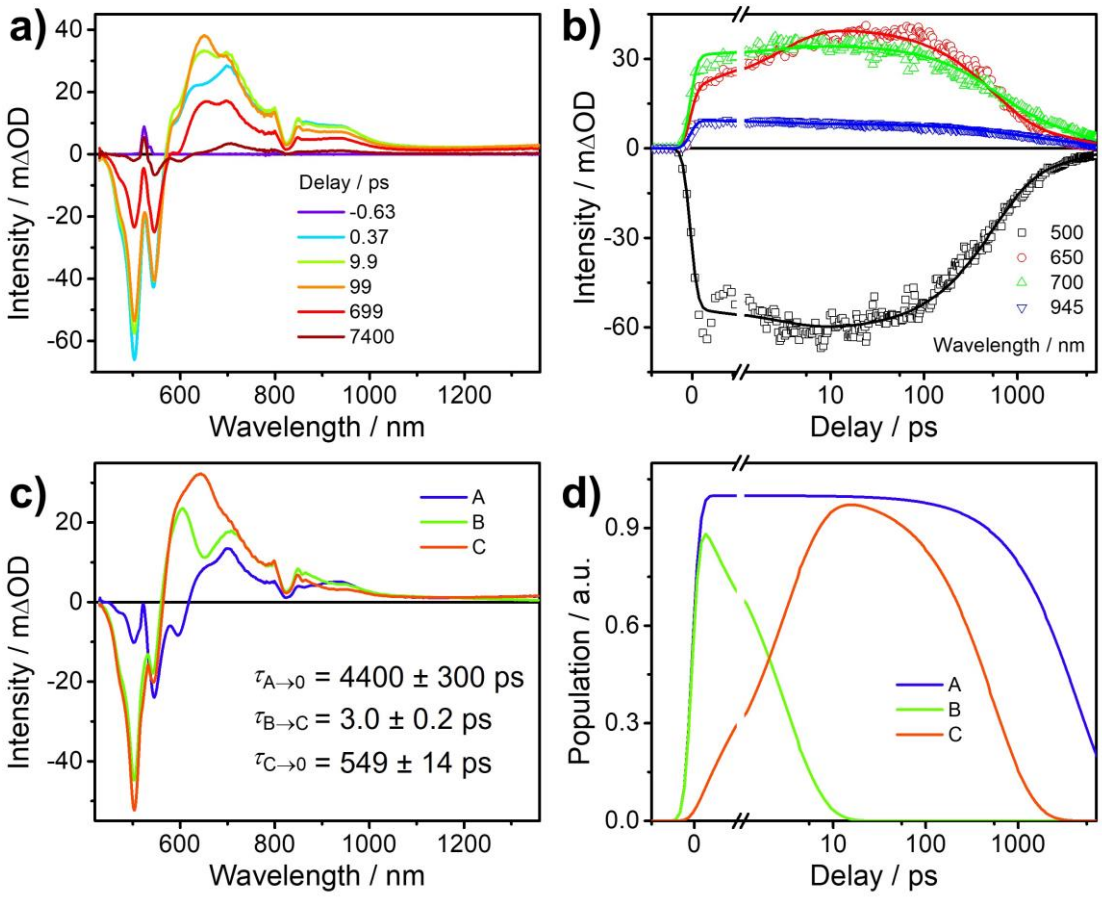

Fig. S14. Femtosecond transient absorption spectra of **PDI-DV-ref** in **H_2O** excited at 525 nm (~100 fs, 1 μJ/pulse). (a) Visible and NIR spectra. (b) Multiple wavelength fits. (c) Species associated spectra and the time constant. (d) Population curve from transient absorption fit to first order decay model. Species A represents the initially prepared singlet excited state of monomer-type **PDI-DV-ref,** while species B is that of aggregated population. Species C is the structurally relaxed singlet excited state of aggregated **PDI-DV-ref**. The excited-state evolution of aggregated **PDI-DV-ref** is fitted to a sequential decay model.

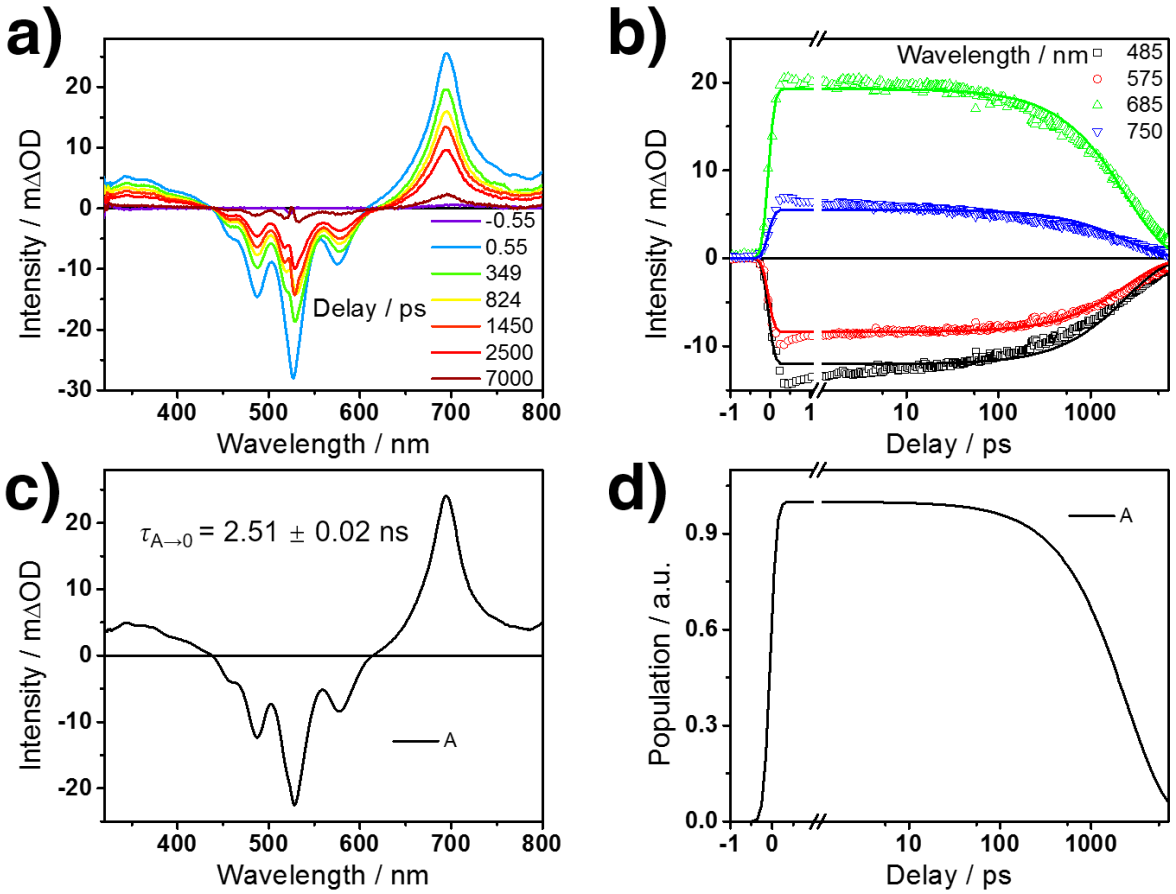

Fig. S15. Femtosecond transient absorption spectra of **PDI-DV** excited at 525 nm (~100 fs, 1 μJ/pulse, **MeCN : H_2O = 75% : 25%**). (a) Visible and NIR spectra. (b) Multiple wavelength fits. (c) Species associated spectra and the time constant. (d) Population curve from transient absorption fit to first order decay model. Species A represents the singlet excited state of **PDI-DV**.

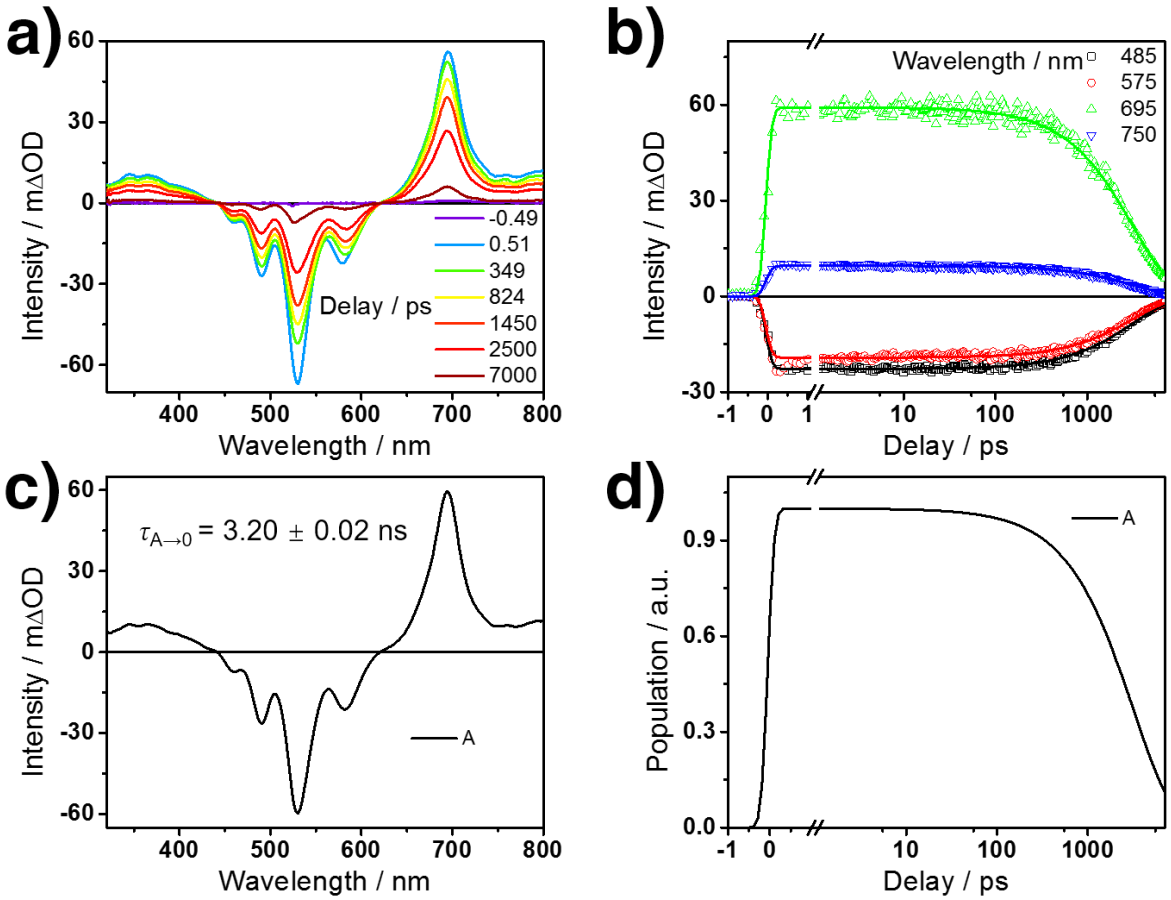

Fig. S16. Femtosecond transient absorption spectra of **PDI-DV** excited at 525 nm (~100 fs, 1 μJ/pulse, **MeCN : H_2O = 50% : 50%**). (a) Visible and NIR spectra. (b) Multiple wavelength fits. (c) Species associated spectra and the time constant. (d) Population curve from transient absorption fit to first order decay model. Species A represents the singlet excited state of **PDI-DV**.

S8. Conductivity Measurements in Humidity Sensing

The gold-interdigitated electrode arrays were fabricated using photolithography on a silicon wafer covered with a 300 nm SiO_2 layer. The gold interdigitated electrode pair was 1 mm in width and 15 μm in gap, and fully covered with the sensor materials via drop-casting. The current change of electrodes was measured by applying a DC voltage of 2V, and the temperature was kept constant at 20℃ during the test.

The conductivity measurements were carried out using a two-probe method on a Signatone S-1160 Probe Station combined with an Agilent 4156C Precision Semiconductor Parameter Analyzer to measure the current response of the humidity sensor. The measurements took place in a shielded dark box to eliminate unwanted light and electromagnetic radiation. A tungsten lamp (Quartzline, 21 V, 150W) was used as the light source for the photocurrent enhancement measurement. The light was guided by an optical fiber and the intensity reaching the sample surface was 60 $mW \cdot cm^{-2}$, as measured by a Melles Griot broadband power/energy meter (model: 13PEM001).

The method to calibrate humidity sensors is the use of saturated salt solutions. At room temperature (20°C), the concentration of a saturated solution is fixed and does not have to be determined. By providing excess solute, the solution will remain saturated even in the presence of modest moisture sources and sinks. When the solute is a solid in the pure phase, it is easy to determine that there is saturation. The saturated salt solution, made up as a slushy mixture with distilled water and chemically pure salt, is enclosed in a glass chamber. The relative humidity and temperature used in this work are summarized in the table below. When testing, the saturated salt solutions were placed in bottles to produce different humidity headspace air where the arrays were placed in to measure the current response.

Table S1. Equilibrium Relative Humidity Saturated Salt Solutions

Compounds	***Relative Humidity* / %**	***Temperature* / *°C***
Potassium Acetate	23.11 ± 0.25	20
Potassium Carbonate	43.16 ± 0.33	20
Sodium Chloride	75.47 ± 0.14	20
Potassium Nitrate	94.62 ± 0.66	20
Pure Water	100	20

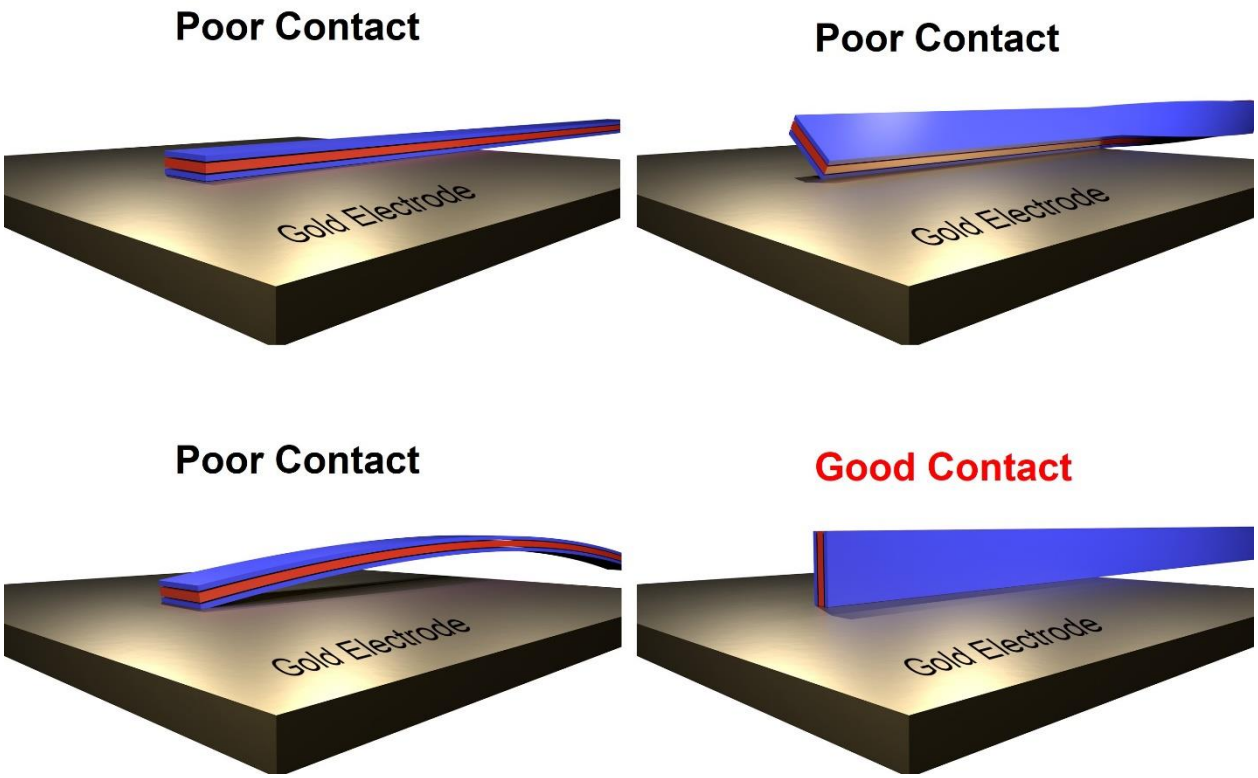

Fig. S17. Different contact modes of the **PDI-DV** nanoribbon fiber and the gold electrode. Only in a few cases can the nanoribbon make good contact with the gold electrode.

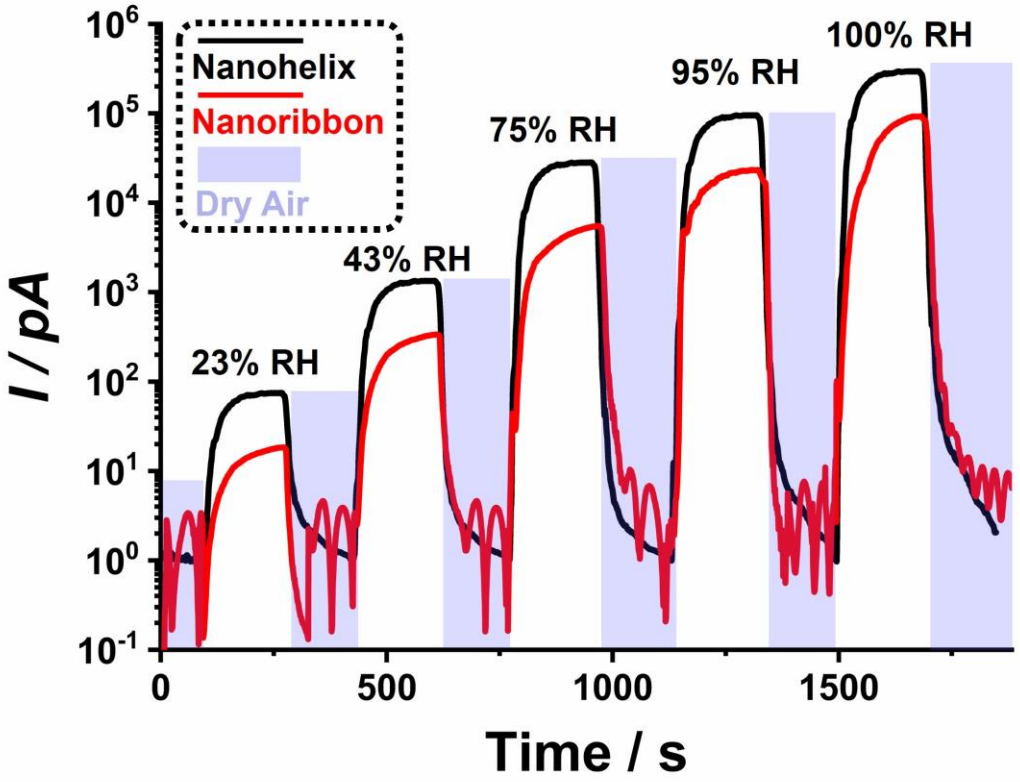

Fig. S18. Current responses of **PDI-DV** nanohelix and nanoribbon fiber to time curves measured at 20 ℃ under different relative humidity.

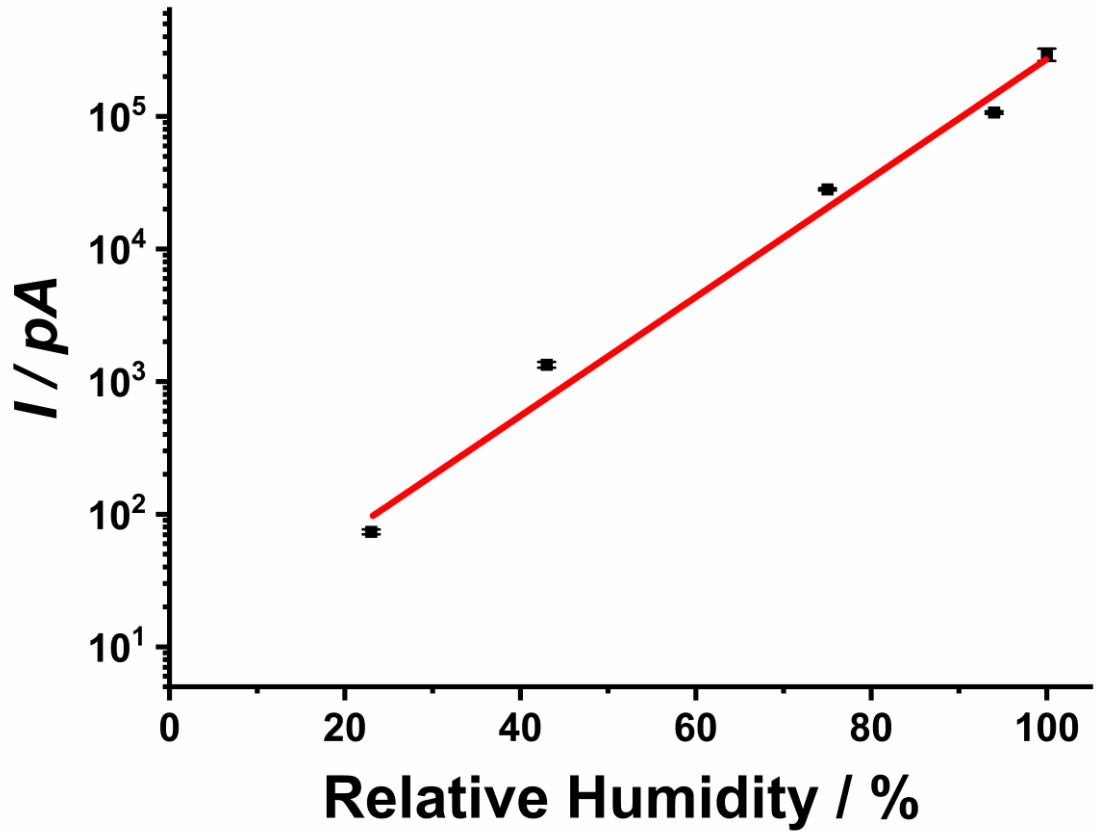

Fig. S19. Dependence of current response on the relative humidity of the **PDI-DV** nanohelix and its fitting diagram.

The equation of the fitting curve is:

$$\ln y = 2.351 + 0.102x \qquad \text{(Eqn. S3)}$$

Where x is the Relative Humidity (%), and y is the current response (pA), $R^2 = 0.984$.

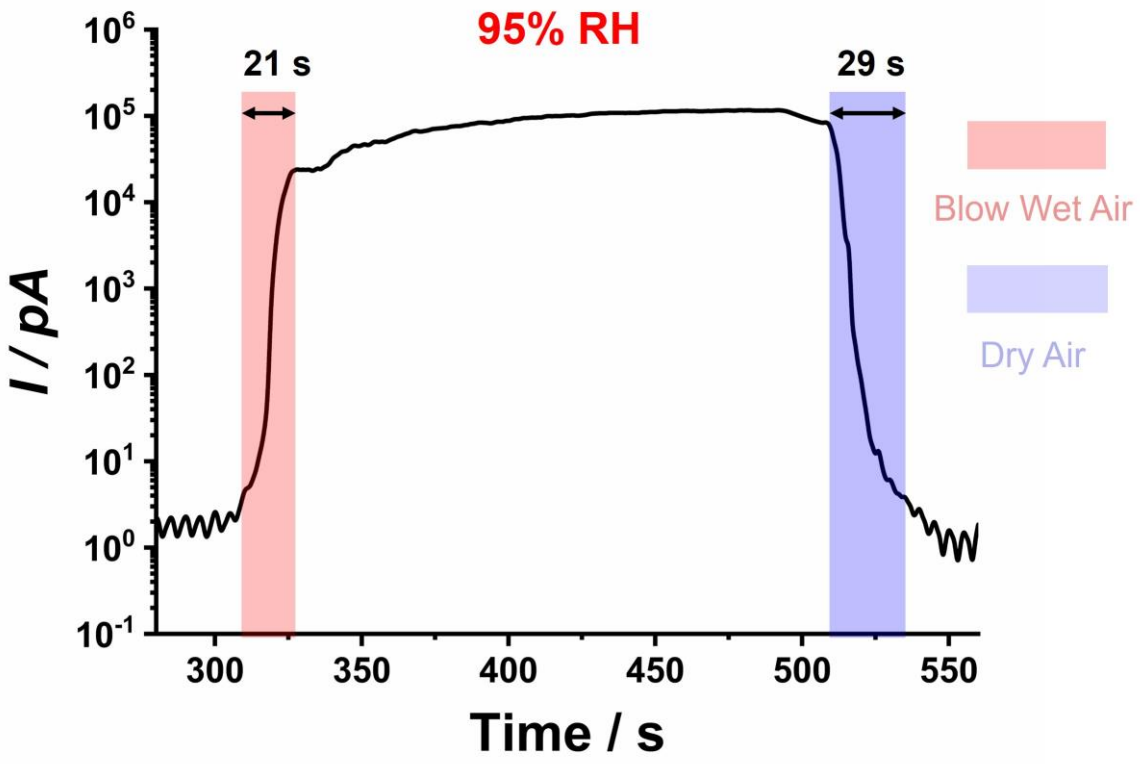

Fig. S20. Response time of **PDI-DV** nanohelix measured at room temperature when blowing 95% RH wet air and dry air.

When testing, the wet headspace air was blowing at a constant velocity to the arrays while measuring the current response, the sensor showed a fast response of 21 s. Then the arrays were placed at static dry air while measuring the current response, the sensor showed fast recovering speed of 29 s.

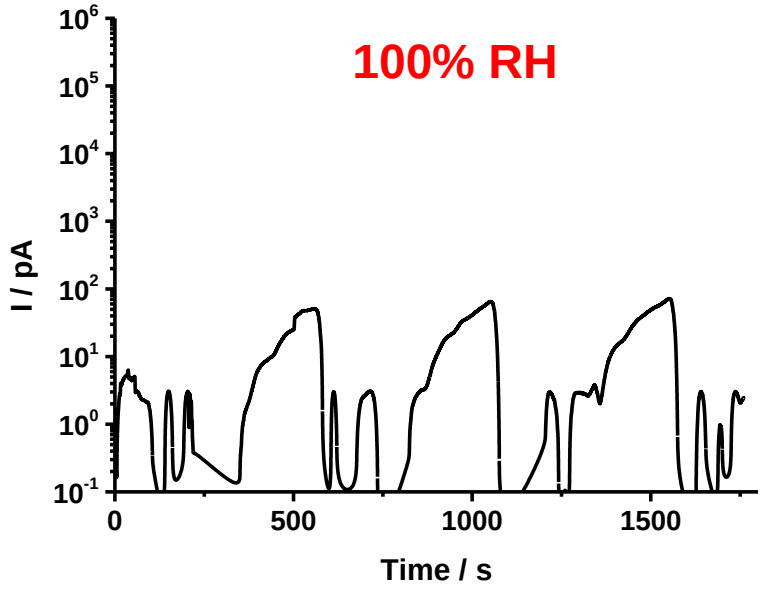

Fig. S21. Current response of reference **DMeV•2PF$_6$** film to time curves measured at room temperature under saturated relative humidity.

Table S2. Performance of the nanohelix sensor in this work compared with the previous work

Sensor materials	***Fabrication method***	***Meas. range***	***Response(I/I_0)***	***Sensitivity***	***Refs***
Keratin	Nanofiber drop-casting	16-82% RH	290.76	4 pF/% RH	4
GO-PEI	Self-assembly layer-by-layer	6.4–97.3% RH	400	37.84 Hz/%RH	5
Ag/SnO_2	Nanocasting	11-98% RH	100000	-1.24 MΩ/% RH	6
Twig-like SnO_2	Hydrothermal	33-98% RH	800	-1.31 kΩ/% RH	7
TEMPO-oxidized cellulose fibers	Self-assembly	11-95% RH	643.8	25 kΩ/% RH	8
NiO–CeO	Self-assembly drop-casting	11-95% RH	100	-45 kΩ/% RH	9
PDI-DV nanohelix	Self-assembly drop-casting	23-100% RH [a]	290000 [ab]	-2.83 MΩ/% RH[a]	This work

[a] Obtained from Fig. S18. [b] 100% RH, I/I_0.

S9. Additional Experimental Details

Specific Surface Area and Pore Size analysis (N_2).

The adsorption experiments were measured with an Autosorb iQ Station 2 outfitted with the micropore option by Quantachrome Instruments, running version 4.0 of the ASWin software package, using the adsorption of N_2 at the temperature of 77.35 K. Prior to measuring, the 0.0057 g nanoribbon and 0.0156 g nanohelix solid sample were degassed at 423.15 K for 2 h and finally outgassed to 10^{-5} Torr.

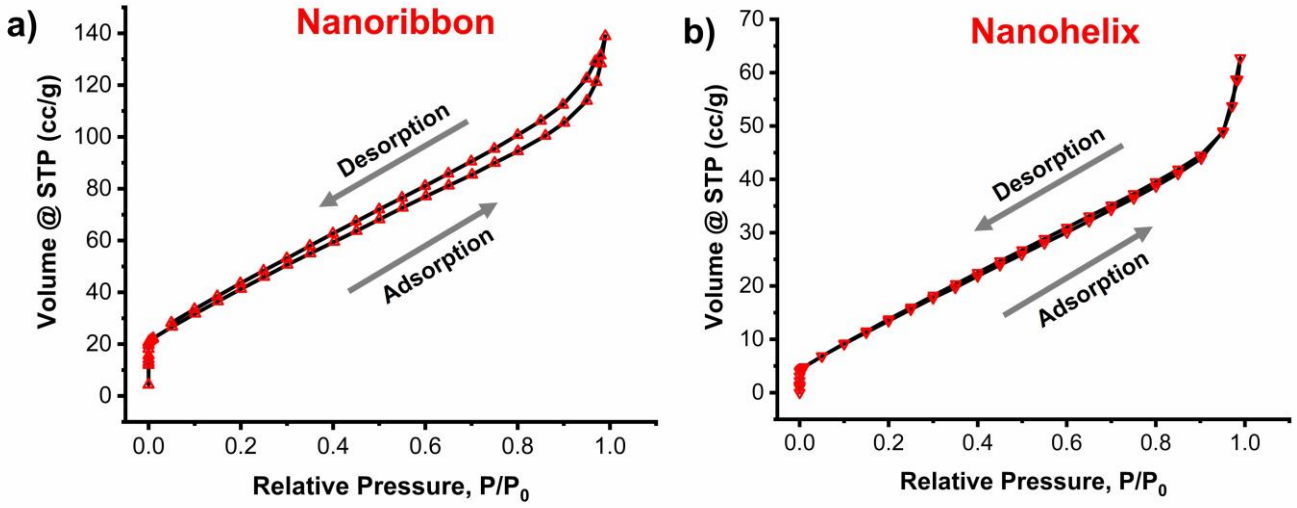

Fig. S22. N_2 adsorption and desorption isotherms at 77.35 K of nanoribbon (a) and nanohelix (b) sample.

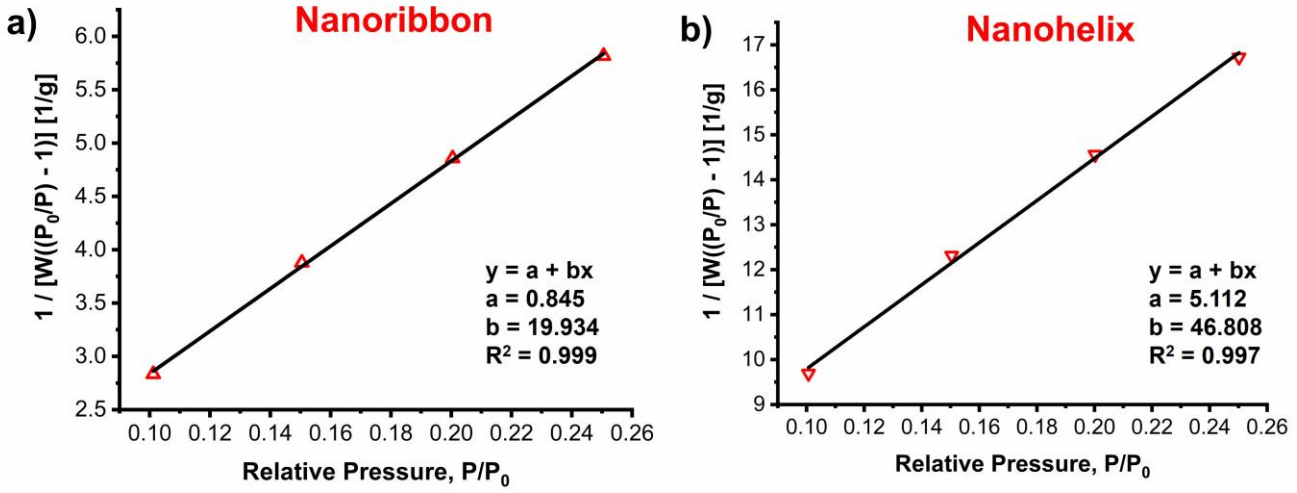

Fig. S23. BET fits for the N_2 adsorption isotherm of the nanoribbon (a) and nanohelix (b) sample.

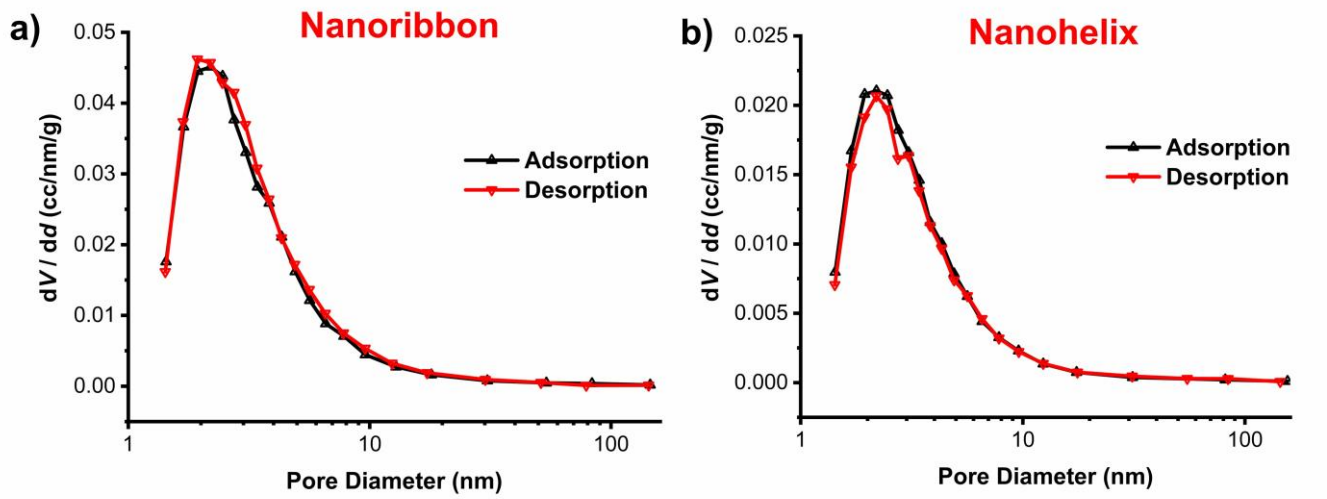

Fig. S24. BJH pore size distributions of nanoribbon (a) and nanohelix (b) sample.

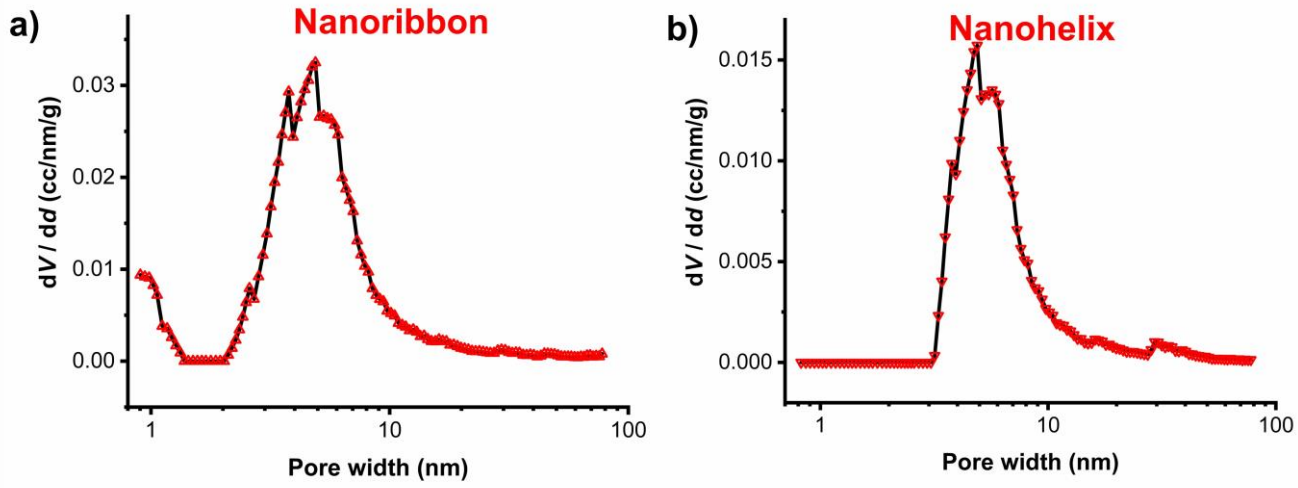

Fig. S25. DFT pore size distributions of nanoribbon (a) and nanohelix (b) sample.

Table S3. Surface Area Analysis of Nanoribbon and Nanohelix Sample

Sample	***BET method***	***BJH method***	***DFT method***
Nanoribbon	167.6 m^2/g	208.95 m^2/g	142.6 m^2/g
Nanohelix	67.07 m^2/g	95.25 m^2/g	45.76 m^2/g

Table S4. Pore Volume Analysis of Nanoribbon and Nanohelix Sample

Sample	*BJH method*	*DFT method*
Nanoribbon	0.2322 cc/g	0.2001 cc/g
Nanohelix	0.1138 cc/g	0.08858 cc/g

Table S5. Pore Diameter Analysis of Nanoribbon and Nanohelix Sample

Sample	*BJH method*	*DFT method*
Nanoribbon	2.064 nm	4.887 nm
Nanohelix	2.190 nm	4.887 nm

Water Vapor Sorption Isotherm.

Water vapor sorption isotherms were measured with an automated Vstar 3-0000-1000-XS from Quantachrome Instruments, running version 1.1.12 of the VstarWin Software package. Prior to measuring, the samples were degassed at 353.15 K for 30 h and finally outgassed to 10^{-5} Torr, approximately 0.0059 g nanoribbon and 0.0055 g nanohelix sample were measured at a temperature of 298.15 K.

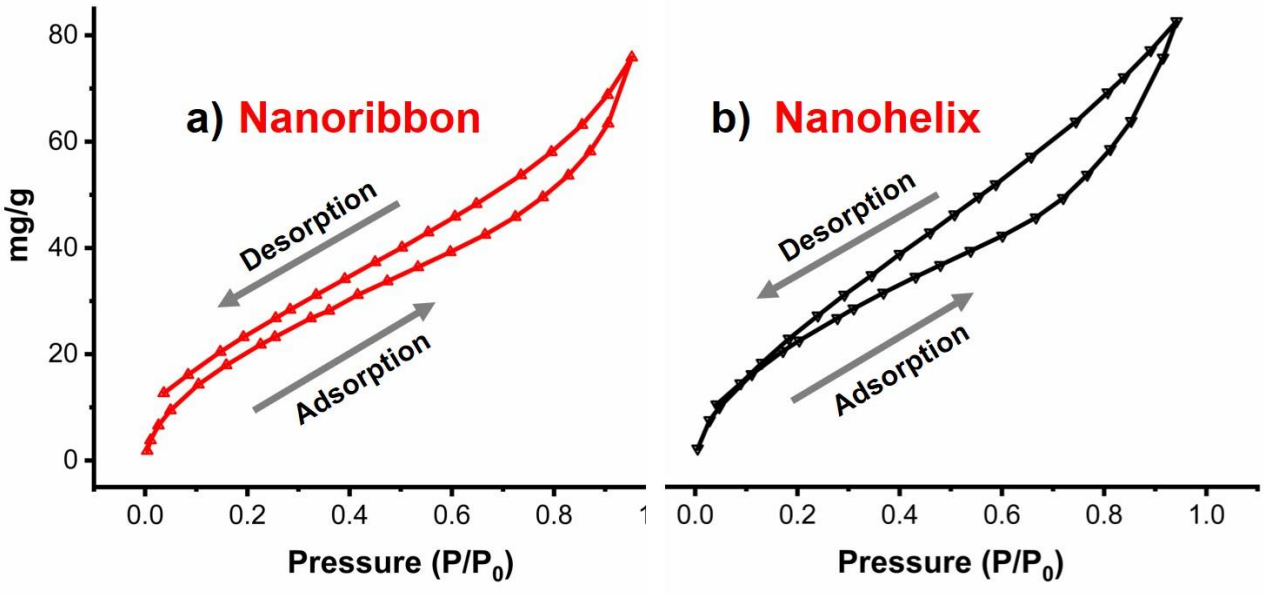

Fig. S26. Water adsorption and desorption isotherms at 298.15 K of nanoribbon (a) and nanohelix (b) sample.

Ascription of waves of cyclic voltammetry in Fig. 3b and 3d.

In the aqueous solution (Fig. 3d), the peak current is given by the Randles-Sevcik equation:

$$i_p = 0.4463nFAC_0(\frac{nFvD}{RT})^{1/2} = \left[0.4463nFAC_0(\frac{nFD}{RT})^{1/2}\right]v^{1/2} \quad \text{(Eqn. S4)}$$

Where:

i_p peak current (A)
n number of electrons
A electrode surface area (cm^2)
C_0 analyte concentration (mol cm^{-3})
v scan rate (V/s)
D diffusion coefficient (cm^2 s^{-1})
F Faraday's constant (C mol^{-1})
R gas constant (J K^{-1} mol^{-1})
T temperature (K)

Simplified formula at room temperature (25 °C):

$$i_p = 2.69\times10^5 n^{3/2} AC_0 D^{1/2} v^{1/2} \quad \text{(Eqn. S5)}$$

where the peak currents in the same measurement (e.g. same electrode area, same scan rate, etc.) are only proportional to $n^{3/2}$, which means a higher peak current implying more electrons transferred. Therefore, based on the equation and the data in Fig. 3d, the well separated peaks at -572 mV and -448 mV can be qualitatively assigned as DV part (two-electron) and PDI part (one-electron), respectively. In the acetonitrile solution (Fig. 3b), current peaks are significantly overlapped, hindering the application of Randles-Sevcik equation. However, the determination of PDI and viologen parts in acetonitrile solution has been well discussed in literature (e.g. *J. Mater. Chem. C*, 2020, 8, 17261 and its references). In the similar structures, viologens can be reduced into their SOMO level before the reduction of PDIs. So in the acetonitrile solution, −326 mV and −402 mV can be assigned as DV part (two-electron) and PDI part (one-electron), respectively.

S10. Supplementary References

1. S.-h. Kim, N. Shim, H. Lee and B. Moon, *J. Mater. Chem.*, 2012, **22**, 13558-13563.
2. Y. Shao, L. F. Molnar, Y. Jung, J. Kussmann, C. Ochsenfeld, S. T. Brown, A. T. B. Gilbert, L. V. Slipchenko, S. V. Levchenko, D. P. O'Neill, R. A. DiStasio Jr, R. C. Lochan, T. Wang, G. J. O. Beran, N. A. Besley, J. M. Herbert, C. Yeh Lin, T. Van Voorhis, S. Hung Chien, A. Sodt, R. P. Steele, V. A. Rassolov, P. E. Maslen, P. P. Korambath, R. D. Adamson, B. Austin, J. Baker, E. F. C. Byrd, H. Dachsel, R. J. Doerksen, A. Dreuw, B. D. Dunietz, A. D. Dutoi, T. R. Furlani, S. R. Gwaltney, A. Heyden, S. Hirata, C.-P. Hsu, G. Kedziora, R. Z. Khalliulin, P. Klunzinger, A. M. Lee, M. S. Lee, W. Liang, I. Lotan, N. Nair, B. Peters, E. I. Proynov, P. A. Pieniazek, Y. Min Rhee, J. Ritchie, E. Rosta, C. David Sherrill, A. C. Simmonett, J. E. Subotnik, H. Lee Woodcock Iii, W. Zhang, A. T. Bell, A. K. Chakraborty, D. M. Chipman, F. J. Keil, A. Warshel, W. J. Hehre, H. F. Schaefer Iii, J. Kong, A. I. Krylov, P. M. W. Gill and M. Head-Gordon, *Phys. Chem. Chem. Phys.*, 2006, **8**, 3172-3191.
3. H. Langhals, J. Karolin and L. B-Å. Johansson, *J. Chem. Soc., Faraday Trans.*, 1998, **94**, 2919-2922.
4. H. Hamouche, S. Makhlouf, A. Chaouchi and M. Laghrouche, *Sens. Actuator A Phys.*, 2018, **282**, 132-141.
5. Y. Liu, Y. Li, P. Wang, Y. Jin, X. Huang, G. Wei and W. Zeng, *J Mater Sci: Mater Electron*, 2020, **31**, 13229-13239.
6. X. Qu, M.-H. Wang, Y. Chen, W.-J. Sun, R. Yang and H.-P. Zhang, *Mater. Lett.*, 2017, **186**, 182-185.
7. V. K. Tomer and S. Duhan, *Sens. Actuators B Chem.*, 2016, **223**, 750-760.
8. Z. Yuan, H.-L. Tai, Y.-J. Su, G.-Z. Xie, X.-S. Du and Y.-D. Jiang, *Rare Met.*, 2021, **40**, 1597-1603.
9. P. Zhu, Y. Kuang, Y. Wei, F. Li, H. Ou, F. Jiang and G. Chen, *Chem. Eng. J.*, 2021, **404**, 127105.